Active Site Descriptors from ^{95}Mo NMR Signatures of Silica-supported Mo-based Olefin Metathesis Catalysts

Zachariah J. Berkson,[a] Ran Zhu,[b] Christian Ehinger,[a] Lukas Lätsch,[a] Stefan P. Schmid,[a] Darryl Nater,[a] Stephan Pollitt,[a,c] Olga V. Safonova,[c] Snædís Björgvinsdóttir,[a] Alexander B. Barnes,[a] Yuriy Román-Leshkov,[b] Gregory A. Price,[d] Glenn Sunley,[d] and Christophe Copéret*,[a]

[a] *Department of Chemistry and Applied Biosciences, ETH Zürich, Zürich CH-8093, Switzerland*
[b] *Department of Chemical Engineering, Massachusetts Institute of Technology, 77 Massachusetts Avenue, Cambridge, Massachusetts 02139, United States*
[c] *PSI, CH-5232 Villigen, Switzerland*
[d] *Applied Sciences, bp Innovation & Engineering, BP plc, Saltend, Hull, HU12 8DS, UK*

E-mail: ccoperet@ethz.ch
KEYWORDS: Molybdenum, olefin metathesis, heterogeneous catalysis, solid-state NMR spectroscopy

ABSTRACT: The catalytic activity of silica-supported molybdenum oxides for olefin metathesis depends strongly on the metal loading and preparation conditions indicating that the nature and/or amounts of the active sites vary across catalysts. This is illustrated by comparing Mo-based (pre)catalysts prepared by impregnation with different metal loadings (2.5-15.6 wt% Mo) and a well-defined model material (2.3 wt% Mo) prepared via a surface organometallic chemistry (SOMC) synthetic approach. Analyses of FTIR, UV-vis, and Mo K-edge X-ray absorption spectra provide strong evidence that all the (pre)catalysts are composed predominantly of similar isolated Mo dioxo sites; however, they exhibit very different proportions of reducible surface sites and catalytic reaction properties. Specifically, the SOMC-derived catalyst is more active for liquid and gas-phase olefin metathesis conditions than a classical catalyst of similar Mo loading by a factor of 1.5-1.9, depending on precise reaction conditions. Most notably, solid-state ^{95}Mo NMR spectra of these catalysts show distinct features, particularly evident under state-of-the-art high-field (28.2 T) measurement conditions where at least four distinct types of surface Mo dioxo sites are resolved, the distribution of which depends on the preparation methods. In particular, the presence of Mo sites with a specific deshielded ^{95}Mo NMR signal correlates with the catalysts' reducibility and metathesis activity; such sites are most prominent in the SOMC-derived catalyst. First-principles calculations show that the ^{95}Mo NMR parameters, specifically the isotropic chemical shift, δ_{iso}, and quadrupolar coupling constant, C_Q, are good descriptors for local strain and coordination environment: acute (SiO-Mo(O)$_2$-OSi) angles and low coordination numbers at the Mo sites leads to highly deshielded δ_{iso} chemical shifts and small C_Q values, respectively. Orbital and natural chemical shift analyses indicate that the deshielded ^{95}Mo δ_{iso} values of strained species are directly related to low LUMO energies, consistent with their higher reducibility and corresponding reactivity. Overall, this study shows that solid-state NMR is particularly powerful for the identification of distinct supported Mo dioxo species and that their ^{95}Mo chemical shifts are related to their specific local electronic structures, providing a powerful descriptor for the propensity of Mo sites towards reduction and the formation of active sites.

INTRODUCTION

Supported transition metal oxides comprise an important class of heterogenous catalysts with numerous industrial applications.[1–5] Prominent examples include olefin metathesis catalysts used for the valorization of light olefins, e.g. via the Shell Higher Olefin Process (SHOP) and the Lummus Olefin Conversion Technology (OCT) Process),[6,7] which are based on supported Mo and W oxides, respectively (Fig. 1a). These catalysts require relatively high operating temperatures and display rather low overall activity, due mostly to the low quantities of active sites (typically estimated at <5%).[8]

While the precise structure(s) of the catalytic active sites in industrial olefin metathesis catalysts remain unknown, they are thought to correspond to high-valent M(VI) oxo alkylidenes, formed *in situ* from a fraction of the initial dispersed oxo sites. Mo-based systems require significantly lower operating temperatures than their W-based analogues and are less prone to generate inactive bulk metal oxide particles through sintering during the preparation, activation, and regeneration processes. Previous studies of silica-supported Mo oxides have shown that the catalytic activity for propene metathesis depends on Mo loadings, with an optimum at ca. 1 Mo per nm^2.[9] However, the small fractions of active sites suggest that specific (coordination) environments are required for their generation. The presence of proximate Brønsted acid sites, for instance, has been proposed to assist catalyst initiation.[10,11] Furthermore, it has been suggested that the active sites originate from strained and correspondingly high-energy configurations of the tetrahedral Mo dioxo unit, which are more reactive and amiable for conversion into active sites.[9] Yet, little is known about the structures and associated spectroscopic signatures of these sites and the structural differences between active, dormant, or inactive sites. Molecular-level understanding of the structure of the (pre)catalytic active sites has been challenging because of the broad distributions of surface sites and small fractions of active species, as most spectroscopic methods like X-Ray Absorption Spectroscopy (XAS) provide averaged information (*vide infra*).

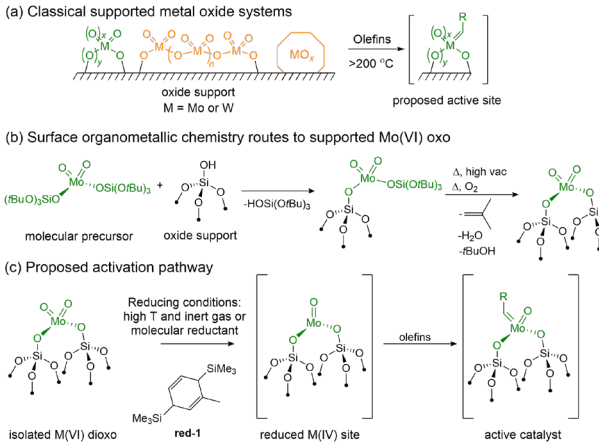

Figure 1. Olefin metathesis catalysts from supported Mo oxo surface sites.

The difficulty of characterization is also associated with the complexity of the surface species. Indeed, conventional catalyst synthesis methodologies such as incipient wetness impregnation (IWI) techniques yield broad distributions of surface species due, in part, to precipitation/dissolution phenomena that occur during synthetic steps carried out in the presence of water.[12] In that context, surface organometallic chemistry (SOMC) has emerged as a powerful method to generate well-defined surface sites from tailored molecular precursors.[13] For example, isolated Mo oxo sites dispersed on highly dehydroxylated silica have been generated by grafting a molecular Mo siloxide precursor followed by a thermolysis step (Figure 1b).[14,15] Mo K-edge XAS analysis supports the presence of highly dispersed Mo(VI) dioxo surface sites that can be readily activated for catalysis at relatively low temperatures (30-70 °C) under reducing conditions (Figure 1c), in particular using a molecular reducing agent.[16,17] In fact, this activation process and associated low temperature activity can also be extended to supported Mo oxide catalysts generated via conventional approaches, albeit with lower activity,[18,19] raising questions about the similitudes and differences between catalysts synthesized via different routes and the precise nature of the (pre)catalytic active sites.

Following the recent development of a methodology to link local geometry, electronic structure, and reactivity based on solid-state ^{95}Mo NMR combined with first-principles orbital analyses, demonstrated on molecular alkyne metathesis catalysts,[20] we examine here silica-supported Mo-based metathesis catalysts prepared by classical and SOMC approaches. While FTIR, UV-vis, and XAS analyses are consistent with the presence of isolated Mo dioxo surface sites as the predominant species in all cases, high-field solid-state ^{95}Mo NMR spectra resolve distinct spectroscopic signatures of different surface Mo sites, whose relative amounts depend on preparation methods and Mo loadings. In particular, this study identifies a correlation between catalyst activity, the reducibility of metal sites, and ^{95}Mo NMR signatures. Detailed first-principles calculations show how coordination geometry affects ^{95}Mo NMR parameters (isotropic chemical shifts and quadrupolar coupling constants) and establish that the most reactive sites, associated with deshielded chemical shifts and small quadrupolar coupling constants, are strained sites with an acute

angle between anionic surface ligands, which are more readily reducible and activated for olefin metathesis.

RESULTS AND DISCUSSION

Catalyst synthesis and characterization. Silica-supported molybdenum oxide (pre)catalysts were synthesized by both IWI and SOMC approaches (Supporting Information, SI section S1.1) on a mesoporous fumed silica support (380 m^2/g) for high metal loading while maintaining appropriate sub-monolayer Mo coverage, thus enabling acquisition of high-quality spectroscopic data. The IWI catalysts were prepared with Mo weight loadings of 2.5 wt%, 4.8 wt%, 7.8 wt%, and 15.6 wt% Mo determined by elemental analysis, corresponding to approximate surface densities of 0.42, 0.80, 1.3, and 2.6 Mo per nm^2. These catalysts are denoted **MoIWI$_{2.5}$**, **MoIWI$_{4.8}$**, **MoIWI$_{7.8}$**, and **MoIWI$_{15.6}$**, respectively. In parallel, a well-defined silica-supported Mo oxo catalyst was prepared by SOMC through the grafting of $[Mo(O)_2(OSi(O^tBu)_3)_2](thf)$ on the same silica support dehydroxylated at 700 °C, followed by consecutive thermal treatments under high vacuum and synthetic air,[17] denoted **MoSOMC$_{2.3}$**. This approach yields a (pre)catalyst with a Mo loading of 2.3 wt% according to elemental analysis. The resulting Mo(VI) oxo sites are isolated and free of organic ligands as previously shown,[17] with a surface coverage of ca. 0.39 Mo per nm^2. The transmission FTIR spectrum of this material (Fig. S2.1) shows features from both isolated and interacting OH groups with relative intensities similar to **MoIWI$_{2.5}$**. Transmission FTIR spectra of the IWI-derived materials (Fig. S2.2) show a decrease in intensity of the signal from isolated Si-OH species as a function of Mo loading, and indicate the presence of H-bonded and/or interacting -OH species in all cases.

Notably, the Mo K-edge X-ray absorption spectra of Mo oxo (pre)catalysts derived from SOMC and IWI are nearly identical (Section S2.2), indicating that the overall structural motifs of the supported Mo oxo sites are the same. The XANES spectra of all of the (pre)catalysts show prominent pre-edge features at ca. 20006 eV, typical of tetrahedral Mo oxides,[22] as well as edge energies at half maximum of ca. 20015 eV, which confirms that the oxidation state is Mo(VI) by comparison to $Mo(VI)O_3$ (Figures S2.3 and S2.4). The EXAFS spectra of the (pre)catalysts are also all very similar (Fig. S2.5), indicating the presence of isolated Mo dioxo sites consistent with previous EXAFS analyses.[16] **MoIWI$_{15.6}$** shows additional features in both EXAFS and XANES regions, which can be attributed to the presence of Mo oxide particles or oligomers at such high Mo loading.[22] The UV-vis spectra of all (pre)catalysts (Figure S2.4) show features at approximately 230 and 280 nm assigned to ligand-metal charge transfer consistent with isolated Mo dioxo sites.[22,23] **MoIWI$_{15.6}$** shows additional broadening out to 400 nm, which has also been attributed to nanocrystalline Mo oxide particles.[23] The XAS and UV-vis spectroscopic features of the (pre)catalysts are thus all mutually consistent and indicate that the predominant Mo surface species in all cases are isolated tetrahedral Mo dioxo sites having two Mo-O-Si linkages to the surface of the silica support, consistent with past computational and spectroscopic studies of molybdenum oxide supported on silica at low loadings.[17,21] **MoIWI$_{15.6}$** additionally possesses a detectable fraction of molybdate polymers and/or clusters formed at high Mo loadings.

Evaluation of catalyst performances. All catalysts were tested for 1-nonene metathesis in liquid-phase batch reactions and propene metathesis in gas phase flow reactions. For the 1-nonene metathesis tests, the catalysts were activated at 70 °C with 2 equiv. of the organosilicon reductant 1-methyl-3,6-bis(trimethylsilyl)-1,4-cyclohexadiene (**red-1**) per Mo in the presence of 1-nonene (1 M concentration, 1000 olefin: 1 Mo). Reactivity tests were run either in open reaction vials to allow for the release of ethylene and higher initial conversions, albeit leading to evaporation and lower conversion, or in closed reaction vials to allow for tracking of reaction kinetics. In open reaction vials, the initial reaction rates per Mo of the IWI-derived catalysts are 7.3×10^{-2}, 8.5×10^{-2}, 7.8×10^{-2}, and 4.3×10^{-2} s^{-1} for **MoIWI$_{2.5}$**, **MoIWI$_{4.8}$**, **MoIWI$_{7.8}$**, and **MoIWI$_{15.6}$**, respectively (Figure 2a, Section S3.1). Notably, the SOMC-derived catalyst exhibits a significantly higher initial activity (11×10^{-2} s^{-1}) on a per Mo basis than any of the IWI catalysts. Similar reaction trends are observed when the reactions are conducted in sealed vials, though with lower initial rates for all catalysts and much lower product selectivities due to post-(metathesis) reactions with ethylene[24,25]

and/or olefin isomerization reactions (Table S3.2). Under these conditions the differences between **MoSOMC$_{2.3}$** and **MoIWI$_{2.5}$** are even more pronounced, showing maximum metathesis product formation rates of 1.5 × 10^{-2} and 0.1 × 10^{-2} (mol product [mol Mo]$^{-1}$ [s]$^{-1}$), respectively. The initial E/Z selectivities of the SOMC and IWI catalysts at low conversion are similar for all catalysts (2.1-3.1), suggesting that all the catalysts have similar active site structures[26] but with different quantities.

Similar but more pronounced trends in reactivity are observed under steady-state gas-phase propene metathesis conditions at 180 °C (Section S3.2). After activation at 500 °C in flowing He, the steady-state propene metathesis rates per Mo are 6.8 × 10^{-4}, 4.1 × 10^{-4}, 14 × 10^{-4}, 2.6 × 10^{-4}, and 0.078 × 10^{-4} s^{-1} for **MoSOMC$_{2.3}$**, **MoIWI$_{2.5}$**, **MoIWI$_{4.8}$**, **MoIWI$_{7.8}$**, and **MoIWI$_{15.6}$**, respectively (Figure 2b, blue). This trend approximately mirrors what is observed for the initial 1-nonene metathesis rates in the liquid phase at 70 °C, albeit the gas phase reaction rates are much lower despite the higher temperatures, possibly pointing to significantly lower amounts of active sites under these activation conditions. In the presence of 1 mol% of a mixture of organic promoter species (85% 2,3-dimethyl-2-butene and 15% 2,3-dimethyl-1-butene, denoted **4MEs**),[11] the steady-state propene metathesis rates increase by 1-2 orders of magnitude for all catalysts (Figure 2b, orange) to 6.7 × 10^{-2}, 3.6 × 10^{-2}, 3.6 × 10^{-2}, 0.57 × 10^{-2}, and 0.062 × 10^{-2} s^{-1} for **MoSOMC$_{2.3}$**, **MoIWI$_{2.5}$**, **MoIWI$_{4.8}$**, **MoIWI$_{7.8}$**, and **MoIWI$_{15.6}$**, respectively, corresponding to enhancement factors of 98, 87, 25, 22, and 80. These enhancements in catalyst activity are similar to values recently obtained for silica-supported W (×26 at 250 °C) and Mo (×30 at 200 °C) oxo catalysts and arise from the ability of the branched promoter olefins to facilitate proton transfers involved in the activation and renewal of catalytic sites.[11] The substantial increase in reaction rates and the very different enhancement factors suggest differences in the numbers of active sites formed as a function of the Mo loading and synthesis method, with all results indicating that the SOMC-derived catalyst has a greater fraction of active sites under most reaction conditions compared to the otherwise similar IWI catalysts. Note that the direct titration of the number of active sites by chemical methods (e.g. cross-metathesis with label compounds) remains a challenge because of the constant formation and loss of active sites under different conditions,[27] leading to different amounts depending on the titrants used.[28] Overall these data indicate that the SOMC synthetic approach is more prone to generate active sites and that the number

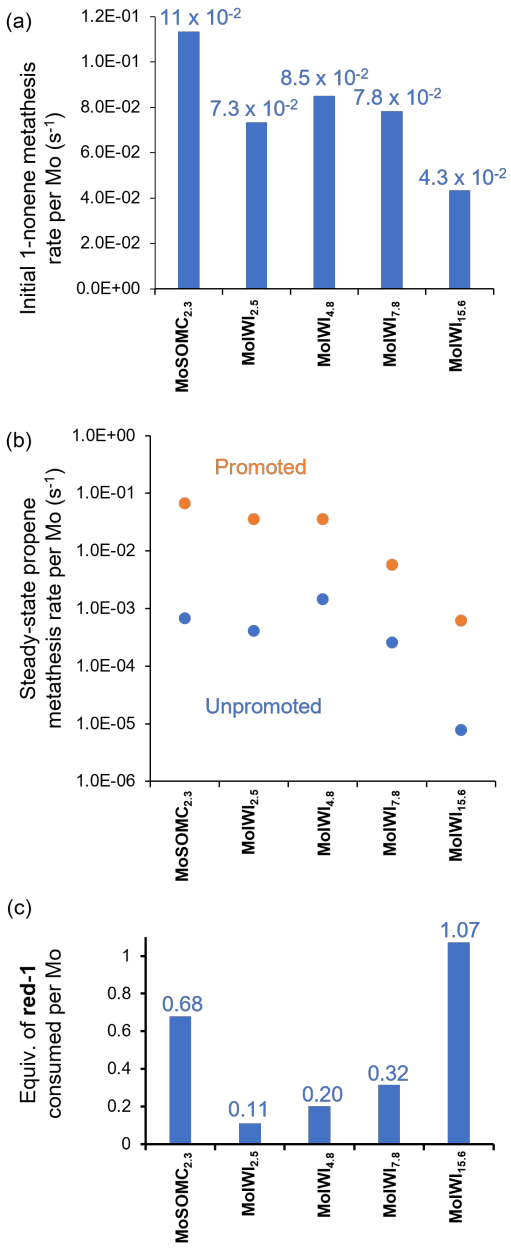

Figure 2. Summary of catalyst reactivity tests. (a) Initial 1-nonene homo-metathesis rates per Mo measured after 10 minutes of reaction time at 70 °C. Reactions were run in open reaction vials under N_2 atmosphere, with 2 equiv. **red-1** per Mo, and 1000 equiv. 1-nonene per Mo in 1,2-dichlorobenzene solvent. (b) Steady-state gas phase propene metathesis reaction rates per Mo either with (orange) or without (blue) 1 mol% **4MEs** promoter. Note the log scale. Catalysts were activated at 400 °C in flowing dry air (3 h), followed by reduction at 500 °C in flowing He (3 h). Reactions were run at 180 °C in 30% propene balanced by He. (c) Equivalents of **red-1** consumed per Mo in each catalyst.

of active sites for the IWI catalysts peaks around 0.8 Mo per nm^2, consistent with literature results.[9] The marked differences in reactivity across these systems is surprising and contrast with the results from Mo K-edge XAS, which suggests a similar average structure for the Mo sites. This led us to further investigate the reactivity and surface structure of the materials.

Reducibility of silica-supported Mo oxo sites. The fraction of reducible Mo(VI) surface sites was estimated by titration with 1.5 equiv. of the organosilicon reductant **red-1** (Section S3.3). Considering that such reductants typically operate via two-electron reduction processes[29] consumption of 1 equiv. **red-1** per Mo is expected for the conversion of Mo(VI) to Mo(IV). Instead, 0.12 and 0.68 equiv. **red-1** are consumed for **MoIWI$_{2.5}$** and **MoSOMC$_{2.3}$**, respectively (Fig. 2c). This suggests a stoichiometric reduction of only 12% and 68% of the total Mo present in these catalysts, respectively, indicating that a substantial fraction of Mo is irreducible. For **MoIWI$_{4.8}$**, **MoIWI$_{7.8}$**, and **MoIWI$_{15.6}$**, 0.17, 0.29, and 1.07 equiv. **red-1** are consumed, respectively, showing that for the IWI series the percentage of reducible Mo sites increases linearly as a function of loading. The high quantity of **red-1** consumed by **MoIWI$_{15.6}$** may be related to the easier reduction of Mo oxide particles/oligomers compared to isolated Mo oxo sites. As **MoSOMC$_{2.3}$** consumes a greater equivalence of **red-1** than any of the IWI catalysts except for **MoIWI$_{15.6}$**, the monodispersed Mo oxo sites generated by the SOMC-based approach are much more readily reducible compared to their counterparts derived from conventional IWI syntheses, despite similar XAS and UV-vis characteristics. In fact, the per-Mo catalytic reactivity correlates reasonably with the estimated fraction of reducible Mo for all the catalysts except **MoIWI$_{15.6}$** (Figure S3.4). This accounts, at least in part, for the higher catalytic activity of **MoSOMC$_{2.3}$** compared to **MoIWI$_{2.5}$** and raises questions regarding the precise differences in the structures of the Mo oxo sites resulting from different synthetic protocols and the relation to reducibility and reactivity.

Surface Brønsted and Lewis acid sites. Since both Brønsted and Lewis acid sites are proposed to be important for olefin metathesis catalytic activity,[11,30] we examined their presence and nature by low-temperature ^{15}N{^{1}H} CPMAS NMR analysis of the fully oxidized (pre)catalysts contacted with ^{15}N-pyridine and desorbed at room temperature. The chemical shift of adsorbed ^{15}N-pyridine readily distinguishes Brønsted (209 ppm) and Lewis acid sites (230-280 ppm) and also enables the strength of the Lewis acid sites to be assessed, with more shielded ^{15}N chemical shifts associated with Lewis acid sites of increasing strength.[31] The ^{15}N{^{1}H} CP-MAS NMR spectra of the pyridine adsorbed (pre)catalysts (Figure 3, Section S4.1) each show isotropic ^{15}N signals at 299, 287, 270, and 209 ppm, though with different relative intensities. The ^{15}N NMR signals at 299-287 ppm (green shaded region) and 209 ppm (blue shaded region) are assigned respectively to pyridine weakly interacting at surface OH sites and pyridinium formed by deprotonation of stronger

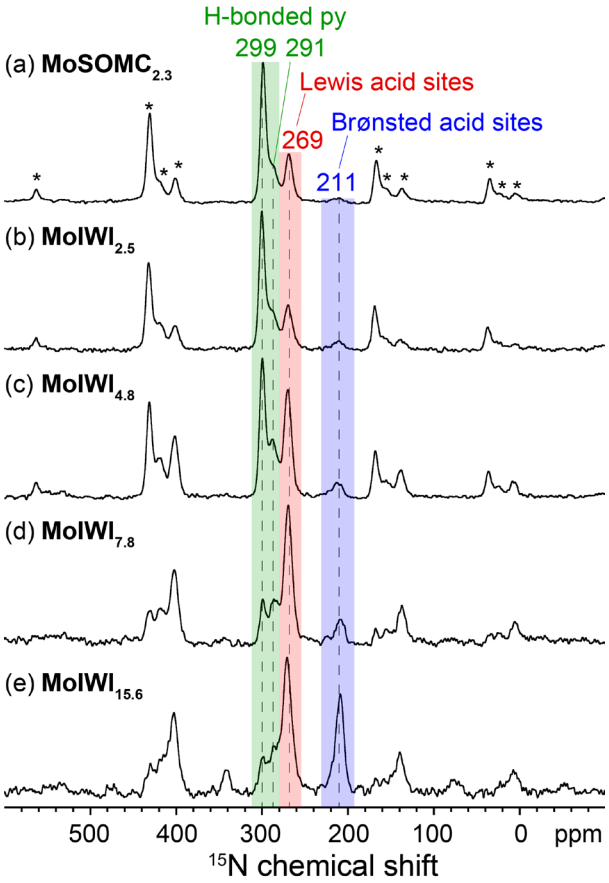

Figure 3. Solid-state 1D ^{15}N{^{1}H} CPMAS NMR spectra of (a) **MoSOMC$_{2.3}$**, (b) **MoIWI$_{2.5}$**, (c) **MoIWI$_{4.8}$**, (d) **MoIWI$_{7.8}$**, and (e) **MoIWI$_{15.6}$** after adsorption of ^{15}N-pyridine and desorption at room temperature under high vacuum. Spectra were acquired at 14.1 T, 8 kHz MAS, 100 K, and with ^{15}N-^{1}H cross-polarization contact times of 2 ms. Asterisks indicate spinning side bands arising from the large ^{15}N chemical shift anisotropy.

Brønsted acid sites, while the ^{15}N NMR signals at 270 ppm (red shaded region) are assigned to pyridine adsorbed at Lewis acid sites, e.g., coordinated to Mo centers. Though not strictly quantitative, the relative integrated ^{15}N signal intensities (Table S4.1) allow relative quantities of Brønsted and Lewis acid sites to be compared across catalysts. Generally, the relative ^{15}N signal intensities from pyridinium and pyridine on strong Lewis acid sites increase as a function of Mo loading while the signals from weakly interacting pyridine decrease. This indicates a nearly linear increase in both Brønsted and strong Lewis acid site density as a function of Mo loading (Figure S4.2), consistent with recent results on similar materials from NH_3 adsorption and FTIR spectroscopy.[32] The two precatalysts with similar Mo loadings prepared via SOMC or impregnation, **MoSOMC$_{2.3}$-py** and **MoIWI$_{2.5}$-py**, exhibit very similar ^{15}N NMR signal intensities, with the SOMC-derived material showing a slightly higher ratio of Brønsted to Lewis acid sites.

Local environments of Mo sites from solid-state ^{95}Mo NMR analysis. Despite their apparent similarities with other characterization techniques, the different supported Mo oxo (pre)catalysts yield distinct ^{95}Mo NMR spectroscopic signatures that are linked to the structure and reactivity of the surface Mo sites. Solid-state ^{95}Mo magic angle spinning (MAS) NMR spectra of the (pre)catalysts acquired at different magnetic field strengths and MAS rates resolve signals from different Mo dioxo species. Specifically, analyses of ^{95}Mo NMR spectra acquired at 14.1 T (600 MHz for ^{1}H) or 28.2 T (1.2 GHz for ^{1}H), the highest stable magnetic field available for solid-state NMR, provide evidence for four spectroscopically distinct Mo oxo species (Figure 4, Section S4.2) with different associated isotropic ^{95}Mo chemical shifts, δ_{iso}, and quadrupolar coupling constants, C_Q. By using 3.2 mm diameter MAS NMR rotors and a combination of techniques for sensitivity enhancement, specifically low-temperature (100 K) measurement conditions, adiabatic double-frequency-sweep (DFS) pulses in the preparatory period,[33] and quadrupolar Carr-Purcell-Meiboom-Gill (QCPMG) detection,[34] high ^{95}Mo NMR signal sensitivity is obtained at 14.1 T for all samples (Fig. 4a,b, Fig. S4.3). Each spectrum shows a broad distribution of ^{95}Mo NMR signal intensity in the -80 to -300 ppm region, consistent with past solid-state ^{95}Mo NMR studies of silica-supported Mo oxides using lower magnetic field strengths;[35,36] however, the ^{95}Mo NMR spectrum of **MoSOMC$_{2.3}$** shows substantially more signal intensity in the deshielded -80 to -100 ppm region compared to **MoIWI$_{2.5}$** (Fig.

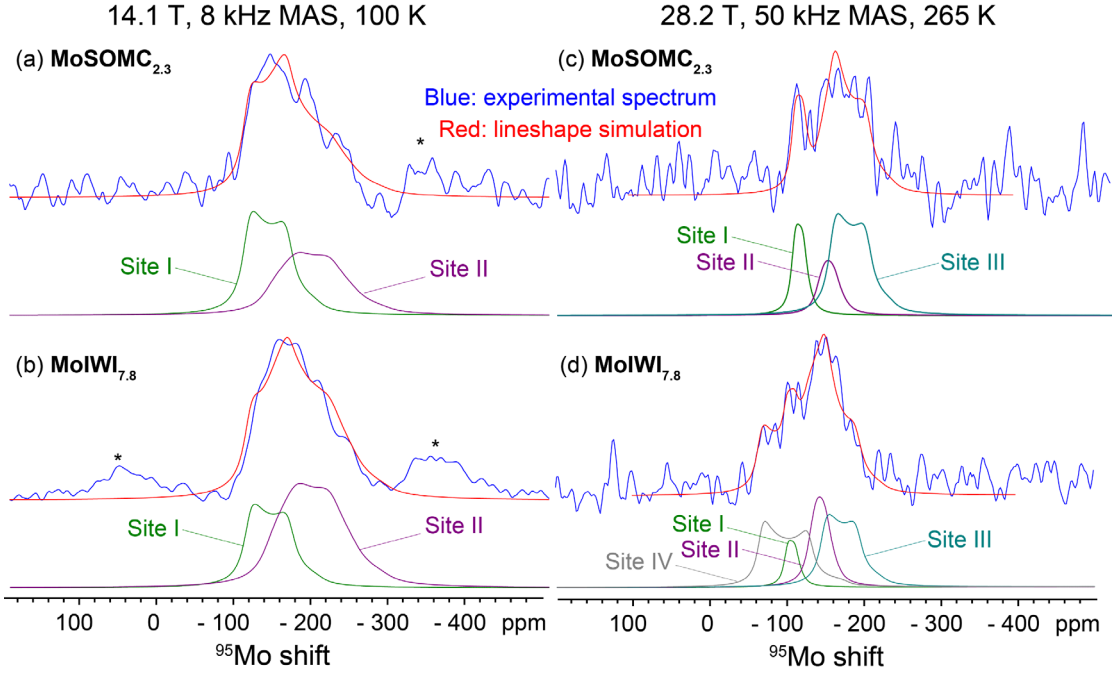

Figure 4. Solid-state ^{95}Mo QCPMG-MAS-NMR reconstructed echo spectra (blue) along with lineshape simulations (red) and spectral deconvolutions of (a, c) **MoSOMC$_{2.3}$** and (b, d) **MoIWI$_{7.8}$**, acquired at (a, b) 14.1 T, 100 K, and 8 kHz MAS or (c, d) 28.2 T, 265 K, and 50 kHz MAS. Asterisks indicate spinning sidebands. See Section S4.1 for complete solid-state ^{95}Mo NMR data.

S4.4a). Signal intensity in this region also increases as a function of Mo loading for the IWI catalysts (Fig. S4.4b). The differences between the SOMC- and IWI-derived catalysts are even more apparent in ^{95}Mo MAS NMR spectra of **MoSOMC$_{2.3}$** and **MoIWI$_{2.5}$** measured at 28.2 T (Fig. 4c,d, Fig. S4.5), where the very high magnetic field strength and fast-MAS conditions yield a much better spectral resolution,[37] albeit with lower signal-to-noise ratios due to the smaller rotor volumes (1.3 mm rotor diameter) and higher temperature (265 K) acquisition conditions. Fitting the experimental ^{95}Mo spectra of all the (pre)catalysts to a minimum number of simulated lineshapes with the same set of spectroscopic parameters (Tables S4.2 and S4.3) provides evidence for four spectroscopically distinct ^{95}Mo species. Specifically, three ^{95}Mo NMR signals are identified for **MoSOMC$_{2.3}$** at 28.2 T: Site I, δ_{iso} ~ -95 ppm and C_Q ~ 3.3 MHz; Site II, δ_{iso} ~ -126 ppm and C_Q ~ 4.0 MHz; and Site III, δ_{iso} ~ -135 ppm and C_Q ~ 6.1 MHz. The same three signals are observed for **MoIWI$_{7.8}$**, along with an additional signal attributed to Site IV, with δ_{iso} ~ -47 ppm and C_Q ~ 7.3 MHz. The ^{95}Mo NMR spectra of all five (pre)catalysts measured at 14.1 T can each be fit to overlapping signals from Site I and Site II (Fig. S4.3), though the spectrum of **MoIWI$_{15.6}$** shows some additional complexity that may be related to the presence of Mo oxide particles as also evidenced by XAS and UV-vis spectroscopy (*vide supra*). Sites III and IV, though likely present in all the IWI-derived (pre)catalysts, are not resolved at 14.1 T, and indeed would be broadened beyond detection due to second-order quadrupolar interactions at the lower field and the larger associated C_Q values of these sites. The resolution of signals from additional high-C_Q ^{95}Mo sites using very high magnetic field strengths (28.2 T) and fast MAS conditions (50 kHz) highlights the power of such state-of-the-art techniques for analysis of catalytic surfaces, especially if signal sensitivity can be improved further, for instance by hyperpolarization[38–40] and/or indirect detection[41] methods.

Overall, the ^{95}Mo MAS NMR spectra resolve important differences between the SOMC-derived (pre)catalyst **MoSOMC$_{2.3}$** and the other materials, specifically the prominence of the relatively narrow and deshielded signal from Site I. The ratio of the integrated signal intensities of Site I and Site II in the spectra measured at 14.1 T are approximately 0.96, 0.30, 0.64, 0.54, and 0.49 for **MoSOMC$_{2.3}$**, **MoIWI$_{2.5}$**, **MoIWI$_{4.8}$**, **MoIWI$_{7.8}$**, and **MoIWI$_{15.6}$**, respectively. Notably, the relative fraction of Site I correlates reasonably well with the observed catalyst reactivity and the fraction of reducible sites measured by **red-1** titration for all catalysts except **MoIWI$_{15.6}$** (Fig. S4.6), suggesting that Site I is responsible for both the greater reducibility and reactivity of **MoSOMC$_{2.3}$**. The large differences in ^{95}Mo δ_{iso} and C_Q values for Mo sites of nominally the same stoichiometry (i.e. Mo dioxo with two siloxide linkages) suggest significant differences in the local structure of the Mo centers of the (pre)catalysts, which we hypothesize are linked to their reactivity.

Relating structure, electronics, and spectroscopic parameters of Mo oxo surface sites. To assess the possible origins of these different NMR signatures and establish the specific relations of geometry, electronic structure, and ^{95}Mo NMR parameters we turned our attention to first-principles calculations based on density functional theory (DFT). Calculated chemical shielding tensor components (σ_{ii}) are related to experimentally measured chemical shifts (δ_{ii}) by the relation $\delta_{ii} = \frac{\sigma_{ref} - \sigma_{ii}}{1 - \sigma_{ref}}$, where σ_{ref} is the chemical shielding of a reference compound. To verify the accuracy of our calculations, calculated parameters were benchmarked on the experimental solution and/or solid-state ^{95}Mo NMR spectra of a reference library of 10 monomeric molecular Mo(VI) mono and dioxo compounds[42–44] (Section S5). Molecular geometries for the reference compounds were optimized using the B3LYP[45] functional in combination with the 6-31g(d)[46] and lanl2dz[47] basis sets for main group and transition metal elements, respectively. The anisotropic chemical shielding (σ) and electric field gradient (efg) tensors were calculated (Section S6.1) with the ADF 2019 code using revised Perdew-Burke-Entzerhof functional[48] in combination with TZ2P and QZ4P[49] basis sets for main group elements and Mo, respectively, with the all-electron relativistic zeroth-order regular approximation (ZORA)[50] in its spin-orbit two-component form. Linear correlation to experimental results (Section S6.2) shows excellent agreement between calculated ^{95}Mo σ_{iso} and measured ^{95}Mo δ_{iso} values (Fig. S6.1). Calculated quadrupolar coupling constants were higher than the measured values by 0.2-1.6 MHz (Tables S5.2 and S6.1), which can be attributed to the influence of dynamic averaging of efg tensors as previously observed.[20,51]

We then sought to understand the parameters that drive the ^{95}Mo chemical shift and C_Q values of Mo dioxo sites by computationally screening their response to ligand geometry and the number and types of coordinating ligands. Simplified computational models for Mo dioxo surface sites having the structure $[Mo(O)_2(OSiF_3)_2]L_n$ were considered, where L = a neutral coordinating ligand (e.g., dimethyl ether) as a model for a surface siloxane moiety, and n = 0, 1, or 2. (SiO-Mo(O)$_2$-SiO) angles (α) were systematically varied (Fig. 5a) while all atom positions were allowed to relax. The (O=Mo=O) angle was generally unaffected, varying only 3° (from 107.6° to 104.6°) when α was changed from 87.5° to 135.0°. Overall, several trends are observed (Figure 5b,c,d, Section S6.3): increasing coordination number generally deshields the ^{95}Mo δ_{iso}, as does decreasing α. As α is decreased below the relaxed value for the n = 0 model (ca. 107°), ^{95}Mo C_Q increases. In this regime, the addition of neutral coordinating ligands increases C_Q as well. When α is increased above 107°, the C_Q also tends to increase, though in this regime adding additional neutral ligands typically decreases C_Q. Similar trends are observed for a range of models of Mo dioxo surface sites, including models bearing neutral silanol or siloxane L ligands and molybdasiloxane rings of different sizes (Section S6.4).

Based on these trends, we can establish the primary differences between the four ^{95}Mo species observed in the different Mo oxo precatalysts. The signal from Site I (δ_{iso} ~ -91, C_Q ~ 3.3 MHz), the presence of which appears to be related to catalytic activity, shows a smaller ^{95}Mo C_Q than the other species, suggesting a low-coordinate tetrahedral site. Meanwhile, the relatively deshielded δ_{iso} value indicates an α(SiO-Mo(O)$_2$-SiO) angle of ca. 90° by comparison to the simplified computational models. Thus, we assign Site I to a low-coordinate, "strained" surface site with an acute (SiO-Mo(O)$_2$-SiO) angle. Site II (δ_{iso} ~ -126, C_Q ~ 4.0 MHz) most likely corresponds to a 'relaxed' tetrahedral surface site with one or two coordinated siloxane moieties. Site III (δ_{iso} ~ -135, C_Q ~ 6.1 MHz) does not directly resemble any of the simplified small models, but its ^{95}Mo NMR parameters are similar to the ^{95}Mo NMR signal of the silica-supported Mo oxo siloxide $Mo(O)_2(OSi(O^tBu)_3)_2/SiO_{2\text{-}700}$ (δ_{iso} ~ -150, C_Q ~ 5.0 MHz, Section S5.5) as well as calculated

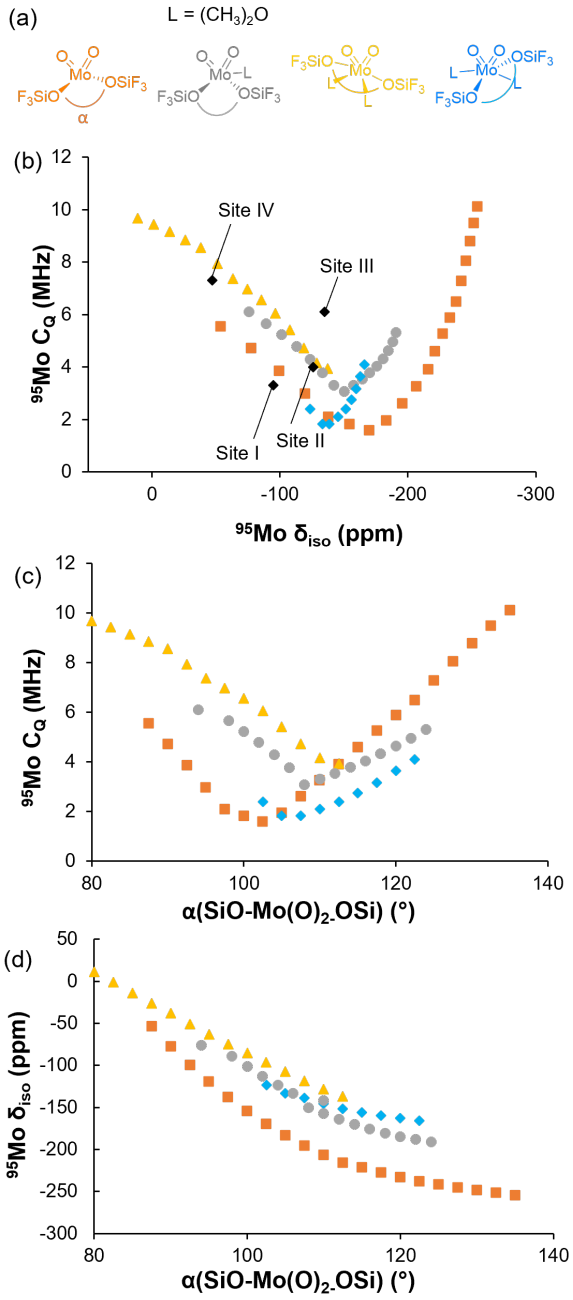

Figure 5. (a) Simplified computational models for Mo dioxo sites with different coordination numbers. (b) ^{95}Mo C_Q v. δ_{iso}, (c) ^{95}Mo δ_{iso} v. α(SiO-Mo(O)$_2$-OSi), and (d) ^{95}Mo C_Q v. α(SiO-Mo(O)$_2$-OSi) for models without a neutral coordinating ligand (orange), with one neutral ligand L = O(CH$_3$)$_2$ (grey), or with two neutral ligands in cis (yellow) or trans (blue) configurations.

models having coordinated neutral siloxane or silanol ligands (Fig. S6.3). The high C_Q and shielded δ_{iso} values of Site III indicate a high coordinate surface site with a relatively large (SiO-Mo(O)$_2$-OSi) angle and at least one coordinated neutral ligand such as a surface siloxane bridge. The highly deshielded signal from Site IV (δ_{iso} ~ -47, C_Q ~ 7.3 MHz), only detected for **MoIWI$_{7.8}$** at 28.2 T because of the large C_Q, is most plausibly a hexacoordinate Mo dioxo site, though a small quantity of oxidic nanoparticles or clusters with signals in this region[35,52,53] may be present at these relatively high Mo loadings and cannot be excluded. Overall, the ^{95}Mo NMR parameters provide highly resolved structural insights into the supported Mo oxo species and show that each of the (pre)catalysts exhibits a distribution of Mo dioxo sites with several different geometries and coordination environments.

Notably, we have recently shown that ^{95}Mo chemical shifts directly probe the electronic structure of homogeneous Mo alkylidyne catalysts for alkyne metathesis,[20] responding to the positions of HOMO and LUMO as well as the HOMO-LUMO gap and thereby providing a direct experimentally accessible link to reactivity. Since geometric strain has been invoked in the reactivity of supported Mo oxo catalysts,[9] we hypothesized that ^{95}Mo chemical shifts can here provide a link between ligand geometry, positions of frontier molecular orbitals (FMOs) and, correspondingly, reactivity. Indeed, for the simplified model [Mo(O)$_2$(OSiF$_3$)$_2$], a strong relation is observed between calculated LUMO energy and α(SiO-Mo(O)$_2$-OSi) (Figure 6a) as well as ^{95}Mo δ_{iso} (Figure 6b). Very similar relations are observed for the five- and six-coordinate models (Section S6.5). As α values are decreased below 115° (increasing strain), the LUMO energy decreases nearly linearly. The HOMO-LUMO gap for these compounds is driven primarily by the decrease in the LUMO energy as the HOMO energy is nearly constant (Section S6.5), being localized on the oxo ligands (*vide infra*), the geometry of which changes very little. A strained geometry around the metal center thus results in decreasing LUMO energy, consistent with the higher reducibility of Mo and greater reactivity of the surface species, as well as more deshielded ^{95}Mo chemical shifts. Indeed, a similar link between ^{95}Mo chemical shifts and reducibility was recently found for molecular Mo(VI) oxo compounds with different (fluor)alkoxy ligands.[43] The manifestation of this effect in the ^{95}Mo chemical shifts of surface species provides an experimental link between their geometry, electronic structure, and reactivity, which can be directly accessed and used to assess the performance of heterogeneous catalyst materials.

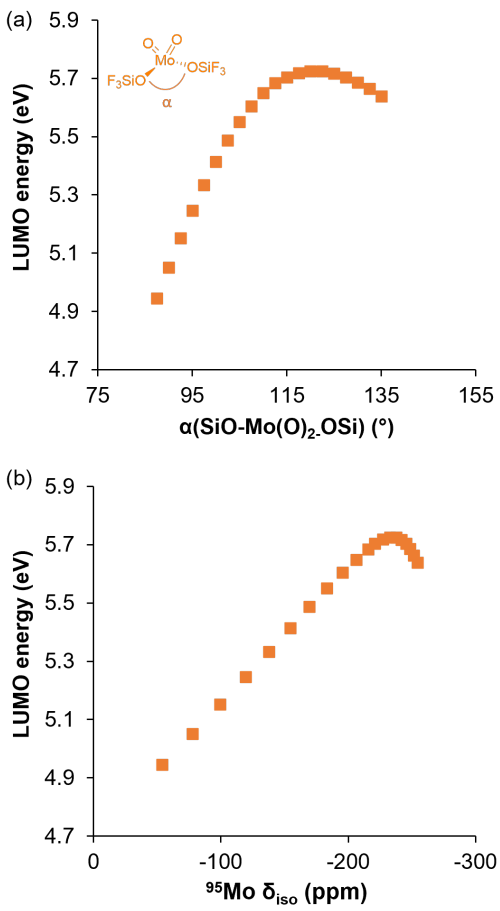

Figure 6. Calculated LUMO energy as a function of (a) α(SiO-Mo(O)$_2$-OSi) angle and (b) ^{95}Mo δ_{iso} for [Mo(O)$_2$(OSiF$_3$)$_2$] models.

Orbital analysis of ^{95}Mo NMR chemical shifts and links to electronic structures. The components of the chemical shielding tensor can be decomposed into diamagnetic and paramagnetic as well as spin orbit contributions ($\sigma_{ii} = \sigma_{ii,dia} + \sigma_{ii,para+SO}$).[60] The diamagnetic contribution is typically constant for a given nucleus.[60] Changes in the chemical shielding arise mostly from $\sigma_{ii,para+SO}$, which the Ramsey equation[60] (Fig. 7a) relates to the overlap of filled/occupied (Ψ_{occ}) and virtual/vacant (Ψ_{vac}) orbitals that are coupled by the angular momentum operator $\hat{L}_i$ of the principal axis i. Since $\sigma_{ii,para+SO}$ is inversely proportional to the energy difference between these occupied and vacant orbitals, $\Delta E_{vac-occ}$, the closer the orbitals are in

energy, the greater the deshielding of the corresponding chemical shielding tensor component. Orbital analyses of chemical shift tensor components have been used to understand reactivity patterns of coordination compounds, mostly focusing on the chemical shift/shielding tensors of nuclei in ligand atoms bound to a metal center.[54–59] Our most recent work on molecular Mo-based alkyne metathesis catalysts showed that orbital analysis of chemical shifts/shielding tensors of metal nuclei (i.e. ^{95}Mo) can provide more direct links to the frontier molecular orbitals (FMOs) involved in reactivity.[20]

In order to relate local geometry and ^{95}Mo chemical shift tensors in the Mo dioxo complexes discussed above, we performed DFT calculations of a smaller computational model, $[Mo(O)_2(F)_2]$, where α(F-Mo(O)$_2$-F) angles were set to 87.5°, 107.5°, or 135.0°. This further simplified ligand set was chosen to facilitate orbital analysis. The relation between geometry and ^{95}Mo chemical shielding tensors follows the same trend as for the $[Mo(O)_2(OSiF_3)_2]$ series (Section S6.6), with σ_{iso} becoming more deshielded with decreasing α(X-Mo-X). Also like the $[Mo(O)_2(OSiF_3)_2]$ series, the ^{95}Mo σ_{iso} is largely driven by changes in σ_{11}, which is oriented between the two oxo ligands and defines the *z* axis (Figure 7b).

Orbital analysis of the ^{95}Mo chemical shielding tensors, based on symmetry arguments anchored on group theory, reveals the specific relations of geometry, FMOs, and chemical shift response. From natural chemical shift (NCS) and natural bonding orbital (NBO) analyses (Section S6.7), the occupied natural localized molecular orbitals (NLMOs) that contribute most to the ^{95}Mo σ_{11} of $[Mo(O)_2F_2]$ (C_{2v} symmetry) are the σ(Mo–O) NLMOs followed by π(Mo–O) NLMOs (Figure 7c,d, Fig. S6.10, Fig. S6.11). Both these contributions to σ_{11} decrease in magnitude with increasing α(F-Mo-F) angle (Figure 7d). Multiple d orbitals contribute to σ(Mo–O), specifically $d_{x^2-y^2}$ and d_{yz}; similarly, d_{xy} and d_{xz} orbitals contribute to π(M–O)

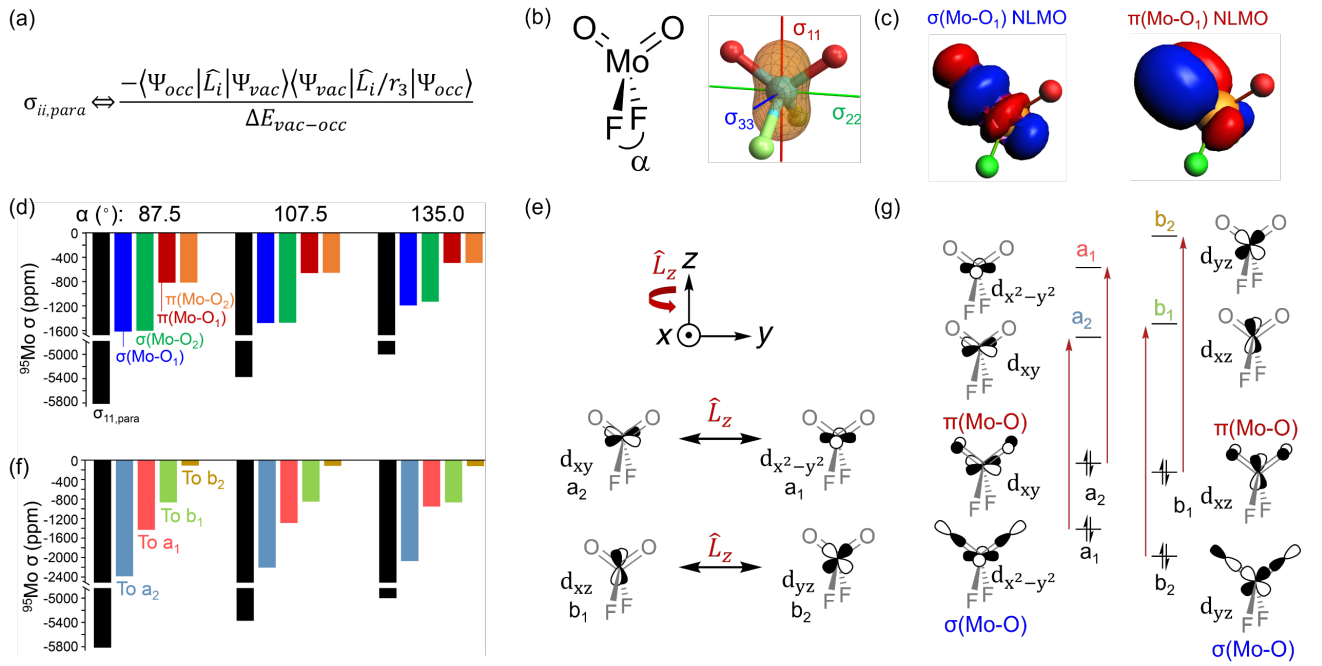

Figure 7. Summary of orbital analysis of ^{95}Mo chemical shielding tensors. (a) Ramsey equation relating chemical shielding to the overlap of occupied and vacant orbitals and the energy difference between these orbitals. (b) ^{95}Mo chemical shielding tensor orientation for $[Mo(O)_2F_2]$. (c) Relevant NLMOs. (d) Contributions to the ^{95}Mo σ_{11} for $[Mo(O)_2F_2]$ models with different α(F-Mo(O$_2$)-F) angles arising from the occupied NLMOs shown in (c). (e) Orbital couplings relevant to the ^{95}Mo chemical shielding. (f) Contributions of virtual orbitals of given symmetry to the ^{95}Mo σ_{11} for $[Mo(O)_2F_2]$ models with different α(F-Mo(O$_2$)-F) angles. (g) Simplified excerpt of the MO diagram showing the couplings from occupied to virtual orbitals. See Section S6.7 for details of the orbital analysis.

(Fig. 7c). The symmetry of the coupled virtual orbitals can then be deduced using group theory. Considering that $\hat{L}_z$ is of a_2 symmetry in the C_{2v} point group (Table S6.10), orbitals of irreducible representation a_i can only couple to those of representation a_j, while b_i can only couple to b_j, with i=(1,2) and j=(2,1). Hence, the occupied orbitals contributing to σ(Mo–O) NLMOs, $d_{x^2-y^2}$ (or d_{yz}) with a_1 (or b_2) symmetry, will only couple to virtual orbitals with a_2 (or b_1) symmetry, namely d_{xy} (or d_{xz}). On the other hand, occupied orbitals contributing to π(Mo–O) NLMOs, e.g. d_{xy} (or d_{xz}) with a_2 (or b_1) symmetry, will only couple to virtual orbitals with a_1 (or b_2) symmetry, namely $d_{x^2-y^2}$ (or d_{yz}). These couplings are depicted in Figure 7e. Note that the HOMO, with b_2 symmetry (Figure S6.13), does not contribute to the σ_{11} component of the ^{95}Mo chemical shielding tensor, since it corresponds to lone pairs on the oxo ligands and has no metal-based character. Although the d_{z^2} orbital (a_1 symmetry) would not be expected to contribute to the ^{95}Mo σ_{11} because it is oriented along the *z*-axis, it is mixed with other a_1 symmetric orbitals, modulating their contribution as a function of α(F-Mo-F) angle (see Figures S6.12 and S6.13 and accompanying discussion).

Examining all 17 FMOs (12 occupied, mostly based on ligand p-orbitals, and 5 virtual, mostly based on metal d-orbitals) as a function of α(F-Mo-F) angle shows that the occupied orbitals remain very similar in energy (Figure S6.15). On the other hand, the energy of the virtual orbitals varies more significantly and, consequently, chemical shielding is mostly affected by the positions of the virtual orbitals. For the ^{95}Mo $\sigma_{11,para+SO}$ (Figure 7f), the virtual orbital with a_2 symmetry (LUMO+1) contributes the most, followed by orbitals with a_1 symmetry (LUMO and LUMO+3, which have mixed character). Increasing α(F-Mo-F) brings the fluoride ligands towards the x,y-plane, leading to a larger overlap between F p orbitals and Mo d_{xy} (a_2) and $d_{x^2-y^2}$ (a_1) orbitals, which increases the energy of the LUMO and nearby virtual orbitals, consequently driving and increasing ^{95}Mo chemical shielding (decreasing chemical shift). The next contributors are the virtual orbitals with b_1 and b_2 symmetry, LUMO+2 and LUMO+4, respectively. Increasing α(F-Mo-F) decreases the overlap between F and the d_{xz} (b_1)/d_{yz} (b_2) Mo orbitals, lowering their energy, which results in a marginal increase of their contribution to the overall σ_{11}. Notably, averaging the contributions to virtual a_2 and b_1 orbitals (coupling to filled orbitals with σ(M–O) character) or a_1 and b_2 orbitals (coupling to filled orbitals with π(M–O) character) gives the same contributions obtained from NCS-NBO analysis from filled σ(M–O) or π(M–O) NLMOs, respectively. These orbital couplings are indicated in Figure 7g.

Overall, the orbital analyses show that the ^{95}Mo chemical shift is mostly driven by the energy of the low-lying virtual orbitals that respond to the position of the anionic X ligands, explaining the strong relation of LUMO energy and local geometry, hence rationalizing the observed trends. Namely, decreasing the α(X-Mo-X) angle and increasing strain at the Mo center decreases the energy of low-lying vacant FMOs, resulting in more deshielded (higher chemical shift) ^{95}Mo NMR signatures of more readily reducible and reactive Mo dioxo sites. The prominence of the deshielded ^{95}Mo NMR signal from Site I in the solid-state ^{95}Mo NMR spectra of **MoSOMC$_{2.3}$** is thus linked to the high fraction of reducible Mo sites as well as the higher catalytic activity of this material.

EPILOGUE

All Mo-based catalysts discussed in this work contain similar isolated Mo dioxo surface sites according to their XAS signatures but show different catalytic olefin metathesis activities. The activity of these catalysts correlates with the intensity of the deshielded ^{95}Mo NMR signal attributed to a specific Site I; these sites are particularly abundant in **MoSOMC$_{2.3}$**, a catalyst prepared via SOMC using highly dehydroxylated silica and a thermolytic molecular precursor.[14] In the corresponding catalysts prepared by impregnation, the amount of these sites increases as a function of Mo loading, but they are present in a significantly lower amount than in the SOMC-derived catalyst at the same Mo loading. Similar trends are found upon titration of the amounts of reducible sites with **red-1**, correlating activity, number of reducible sites, and quantity of site I. Notably, detailed DFT analyses indicate that the deshielded ^{95}Mo chemical shifts of site I best match "strained" Mo sites associated with small α(SiO-Mo-OSi) angles. Small α(SiO-

Mo-OSi) angles lead to low energy LUMOs and thereby increased reducibility, consistent with the experimental correlations between activity, reducibility, and NMR signatures. This shows that high olefin metathesis activity of Mo oxo based catalysts requires "strained" tetra-coordinated Mo sites that are easily reduced, consistent with the proposal that Mo(VI) alkylidenes, the key intermediates for olefin metathesis, are formed via reaction of olefins with low valent Mo(IV) sites that generated via reduction of the Mo(VI) di-oxo precatalytic sites (Fig. 1c).[30] The propensity to form more strained sites by SOMC is likely due to the preparation method that involves the use of highly dehydroxylated silica, which itself exhibits a high fraction of strained siloxane bridges,[61,62] and is carried out in the absence of water that can promote dissolution/precipitation and reorganisation of surface species.

We note also that the relative amounts of reducible sites as measured across the various catalysts, e.g., a factor of ca. 6 greater for **MoSOMC$_{2.3}$** compared to **MoIWI$_{2.5}$**with the same Mo loading, is higher than the differences of their catalytic reaction rates, ca. 1.5-1.9, indicating that other factors are at play. For example, the presence of Brønsted acid sites, evidenced here by solid-state $^{15}N\{^{1}H\}$ CPMAS NMR of pyridine-adsorbed samples, has been proposed to be involved in generating the active high-valent metal(VI) alkylidenes from low-valent M(IV) species.[10,30,63,64] As recently shown for both Mo- and W-based heterogeneous catalysts, this process is dynamic and can be accelerated by the presence of organic mediator species like branched olefins, which act as proton shuttles,[11] yielding almost two orders of magnitude increase in catalytic activity for **MoSOMC$_{2.3}$**. The different propene metathesis enhancement factors observed on addition of branched promoter olefins for the SOMC (×97) and classical catalysts (×22-87) show how the dynamic equilibrium of active and inactive Mo sites, which can be altered by the composition of the gas feed, also depends on the strain and reducibility of surface sites, which depend on the synthetic approach. The mutual spatial proximities of reactive (strained) di-oxo Mo(VI) sites and Brønsted acid sites are also likely keys to generating active sites, a process that can be promoted by olefins. Accessing and tuning such parameters will provide further opportunities to improve catalytic performances.

This study also highlights the power of high-field solid-state ^{95}Mo NMR spectroscopy, which is able not only to identify and distinguish various surface Mo sites but also to relate their signatures to specific electronic structures and coordination environments. While Mo K-edge XAS is not able to distinguish significant differences between the various catalysts prepared in this study, the ^{95}Mo NMR signature of Mo dioxo surface sites is extremely sensitive to their local environments. The ^{95}Mo chemical shifts (δ_{iso}) vary across 200 ppm depending on the α(SiO-Mo-OSi) angles, while the quadrupolar coupling constants (C_Q) provide clear information about the local geometry (tetra-, penta- and hexa-coordinated sites). Furthermore, our computational analyses also indicate that the (O_1=Mo=O_2) angles of the dioxo unit are minimally perturbed by local environment (α) and geometry (coordination number); distinguishing between various di-oxo sites would thus not be possible by Raman spectroscopy, which otherwise can effectively distinguish mono- and di-oxo species.[65]

While the use of multiple complementary characterization techniques is crucial to ascertain the structure of metal (surface) sites, our analyses demonstrate how NMR (like EPR spectroscopy for paramagnetic species) provides unique information about electronic structure because of the symmetry of the magnetic moment operator, $\hat{L}_i$. This operator, with the same symmetry as the rotational operator R_i, probes directly the FMOs of metal sites with σ- and π-symmetries, linking spectroscopic signatures to site-specific descriptors for reactivity. This motivates further applications of such approaches to understand electronic structures and (re)activity of transition metal sites across functional materials such as heterogeneous catalysts.

Supporting Information: experimental section, additional catalyst characterization, catalytic reactivity data, characterization of reference compounds, and additional solid-state NMR and DFT results.

Corresponding Author: * Christophe Copéret: ccoperet@ethz.ch

Acknowledgements. This work was supported by BP plc. Z.J.B. thanks an ETH Career Seed Award as well as ETH+ Project SynMatLab for financial support. C.E. acknowledges the Swiss National Science Foundation (grant 200020B_192050) and the Scholarship Fund of the Swiss Chemical Industry (SSCI). Solid-state NMR measurements were conducted using a 600 MHz (14.1 T) DNP NMR spectrometer and a 28.2 T low-gamma 1.3 mm MAS NMR probehead funded by the SNSF (fund numbers 206021_150710 and 198105). The authors acknowledge SLS for providing beamtime at the SuperXAS beamline (MESQUICK proposal: 20221503).

REFERENCES

(1) *Metal Oxide Catalysis*, 1st Edition; Jackson, S. D., Hargreaves, J. S. J., Eds.; WILEY-VCH Verlag, 2009; Vol. 1–2.
(2) *Metal Oxides in Heterogeneous Catalysis*; Védrine, J. C., Ed.; Elsevier, 2018.
(3) Jia, Q.; Ghoshal, S.; Li, J.; Liang, W.; Meng, G.; Che, H.; Zhang, S.; Ma, Z. F.; Mukerjee, S. Metal and Metal Oxide Interactions and Their Catalytic Consequences for Oxygen Reduction Reaction. *J. Am. Chem. Soc.* **2017**, *139* (23), 7893–7903.
(4) Shu, Y.; Chen, H.; Chen, N.; Duan, X.; Zhang, P.; Yang, S.; Bao, Z.; Wu, Z.; Dai, S. A Principle for Highly Active Metal Oxide Catalysts via NaCl-Based Solid Solution. *Chem* **2020**, *6* (7), 1723–1741.
(5) Fu, J.; Liu, S.; Zheng, W.; Huang, R.; Wang, C.; Lawal, A.; Alexopoulos, K.; Liu, S.; Wang, Y.; Yu, K.; et al. Modulating the Dynamics of Brønsted Acid Sites on PtWOx Inverse Catalyst. *Nat. Catal.* **2022**, *5* (2), 144–153.
(6) Mol, J. C. Industrial Applications of Olefin Metathesis. *J. Mol. Catal. A Chem.* **2004**, *213* (1), 39–45.
(7) Keim, W. Oligomerization of Ethylene to α-Olefins: Discovery and Development of the Shell Higher Olefin Process (SHOP). *Angew. Chemie - Int. Ed.* **2013**, *52* (48), 12492–12496.
(8) Lwin, S.; Wachs, I. E. Olefin Metathesis by Supported Metal Oxide Catalysts. *ACS Catal.* **2014**, *4* (8), 2505–2520.
(9) Amakawa, K.; Sun, L.; Guo, C.; Hävecker, M.; Kube, P.; Wachs, I. E.; Lwin, S.; Frenkel, A. I.; Patlolla, A.; Hermann, K.; Schlögl, R.; Trunschke, A. How Strain Affects the Reactivity of Surface Metal Oxide Catalysts. *Angew. Chemie - Int. Ed.* **2013**, *52* (51), 13553–13557.
(10) Chan, K. W.; Mance, D.; Safonova, O. V.; Copéret, C. Well-Defined Silica-Supported Tungsten(IV)-Oxo Complex: Olefin Metathesis Activity, Initiation, and Role of Brønsted Acid Sites. *J. Am. Chem. Soc.* **2019**, *141* (45), 18286–18292.
(11) Gani, T. Z. H.; Berkson, Z. J.; Zhu, R.; Kang, J. H.; Iorio, J. R. Di; Chan, W.; Consoli, D. F.; Shaikh, S. K.; Copéret, C.; Román-, Y. Universal Promotion of Heterogeneous Olefin Metathesis Catalysts by Controlling Dynamic Active Site Renewal. *Accepted*. Preprint. doi.org/10.33774/chemrxiv-2021-140tk.
(12) Munnik, P.; De Jongh, P. E.; De Jong, K. P. Recent Developments in the Synthesis of Supported Catalysts. *Chem. Rev.* **2015**, *115* (14), 6687–6718.
(13) Copéret, C. Single-Sites and Nanoparticles at Tailored Interfaces Prepared via Surface Organometallic Chemistry from Thermolytic Molecular Precursors. *Acc. Chem. Res.* **2019**, *52* (6), 1697–1708.
(14) Fujdala, K. L.; Tilley, T. D. Design and Synthesis of Heterogeneous Catalysts: The Thermolytic Molecular Precursor Approach. *J. Catal.* **2003**, *216* (1–2), 265–275.
(15) Wegener, S. L.; Marks, T. J.; Stair, P. C. Design Strategies for the Molecular Level Synthesis of Supported Catalysts. *Acc. Chem. Res.* **2012**, *45* (2), 206–214.

(16) Mougel, V.; Chan, K.-W.; Siddiqi, G.; Kawakita, K.; Nagae, H.; Tsurugi, H.; Mashima, K.; Safonova, O.; Copéret, C. Low Temperature Activation of Supported Metathesis Catalysts by Organosilicon Reducing Agents. *ACS Cent. Sci.* **2016**, *2* (8), 569–576.
(17) Yamamoto, K.; Chan, K. W.; Mougel, V.; Nagae, H.; Tsurugi, H.; Safonova, O. V.; Mashima, K.; Copéret, C. Silica-Supported Isolated Molybdenum Di-Oxo Species: Formation and Activation with Organosilicon Agent for Olefin Metathesis. *Chem. Commun.* **2018**, *54* (32), 3989–3992.
(18) Berkson, Z. J.; Bernhardt, M.; Schlapansky, S. L.; Benedikter, M. J.; Buchmeiser, M. R.; Price, G. A.; Sunley, G. J.; Copéret, C. Olefin-Surface Interactions: A Key Activity Parameter in Silica-Supported Olefin Metathesis Catalysts. *JACS Au* **2022**, *2* (3), 777–786.
(19) Copéret, C.; Mougel, V.; Mashima, K.; Tsurugi, H.; Nagae, H. Activation of Supported Olefin Metathesis Catalysts by Organic Reductants, International Patent, Application No. PCT/CH2015/000185. 15 Dec., 2016.
(20) Berkson, Z. J.; Lätsch, L.; Hillenbrand, J.; Fürstner, A.; Copéret, C. Classifying and Understanding the Reactivities of Mo-Based Alkyne Metathesis Catalysts from 95 Mo NMR Chemical Shift Descriptors. *J. Am. Chem. Soc.* **2022**, *144* (33), 15020–15025.
(21) Chempath, S.; Yihua, Z.; Bell, A. T. DFT Studies of the Structure and Vibrational Spectra of Isolated Molybdena Species Supported on Silica. *J. Phys. Chem. C* **2007**, *111* (3), 1291–1298.
(22) Thielemann, J. P.; Ressler, T.; Walter, A.; Tzolova-Müller, G.; Hess, C. Structure of Molybdenum Oxide Supported on Silica SBA-15 Studied by Raman, UV-Vis and X-Ray Absorption Spectroscopy. *Appl. Catal. A Gen.* **2011**, *399* (1–2), 28–34.
(23) Lee, E. L.; Wachs, I. E. In Situ Spectroscopic Investigation of the Molecular and Electronic Structures of SiO 2 Supported Surface Metal Oxides. *J. Phys. Chem. C* **2007**, *111* (39), 14410–14425.
(24) Hoveyda, A. H.; Liu, Z.; Qin, C.; Koengeter, T.; Mu, Y. Impact of Ethylene on Efficiency and Stereocontrol in Olefin Metathesis: When to Add It, When to Remove It, and When to Avoid It. *Angew. Chemie* **2020**, 2–27.
(25) Ivin, K. J.; Mol, J. C. *Olefin Metathesis and Metathesis Polymerization*; Elsevier, 1997.
(26) Copéret, C. Stereoselectivity of Supported Alkene Metathesis Catalysts: A Goal and a Tool to Characterize Active Sites. *Beilstein J. Org. Chem.* **2011**, *7*, 13–21.
(27) Chan, K. W. Understanding the Structure, Activity and Initiation of Active Sites in Tungsten Oxo Based Olefin Metathesis Catalysts, ETH Zürich, 2019. Doctoral thesis. DOI : 10.3929/ethz-b-000395384
(28) Ding, K.; Gulec, A.; Johnson, A. M.; Drake, T. L.; Wu, W.; Lin, Y.; Weitz, E.; Marks, L. D.; Stair, P. C. Highly Efficient Activation, Regeneration, and Active Site Identification of Oxide-Based Olefin Metathesis Catalysts. *ACS Catal.* **2016**, *6* (9), 5740–5746.
(29) Saito, T.; Nishiyama, H.; Tanahashi, H.; Kawakita, K.; Tsurugi, H.; Mashima, K. 1,4-Bis(Trimethylsilyl)-1,4-Diaza-2,5-Cyclohexadienes as Strong Salt-Free Reductants for Generating Low-Valent Early Transition Metals with Electron-Donating Ligands. *J. Am. Chem. Soc.* **2014**, *136* (13), 5161–5170.
(30) Amakawa, K.; Wrabetz, S.; Kröhnert, J.; Tzolova-Müller, G.; Schlögl, R.; Trunschke, A. In Situ Generation of Active Sites in Olefin Metathesis. *J. Am. Chem. Soc.* **2012**, *134* (28), 11462–11473.
(31) Moroz, I. B.; Larmier, K.; Liao, W. C.; Copéret, C. Discerning γ-Alumina Surface Sites with Nitrogen-15 Dynamic Nuclear Polarization Surface Enhanced NMR Spectroscopy of Adsorbed Pyridine. *J. Phys. Chem. C* **2018**, *122* (20), 10871–10882.
(32) Amakawa, K.; Wang, Y.; Kröhnert, J.; Schlögl, R.; Trunschke, A. Acid Sites on Silica-Supported Molybdenum Oxides Probed by Ammonia Adsorption: Experiment and Theory. *Mol. Catal.* **2019**, *478* (August), 110580.
(33) Iuga, D.; Schäfer, H.; Verhagen, R.; Kentgens, A. P. M. Population and Coherence Transfer Induced by Double Frequency Sweeps in Half-Integer Quadrupolar Spin Systems. *J. Magn. Reson.* **2000**, *147* (2), 192–209.
(34) Larsen, F. H.; Jakobsen, H. J.; Ellis, P. D.; Nielsen, N. C. QCPMG-MAS NMR of Half-Integer

Quadrupolar Nuclei. *J. Magn. Reson.* **1998**, *131* (1), 144–147.
(35) D'Espinose De Lacaillerie, J. B.; Gan, Z.; Lacaillerie, J. E. De; Gan, Z. MAS NMR Strategies for the Characterization of Supported Molybdenum Catalysts. *Appl. Magn. Reson.* **2007**, *32* (4), 499–511.
(36) Zheng, H.; Ma, D.; Bao, X.; Jian, Z. H.; Ja, H. K.; Wang, Y.; Peden, C. H. F. Direct Observation of the Active Center for Methane Dehydroaromatization Using an Ultrahigh Field 95Mo NMR Spectroscopy. *J. Am. Chem. Soc.* **2008**, *130* (12), 3722–3723.
(37) Berkson, Z. J.; Björgvinsdóttir, S.; Yakimov, A.; Gioffrè, D.; Korzyński, M. D.; Barnes, A. B.; Copéret, C. Solid-State NMR Spectra of Protons and Quadrupolar Nuclei at 28.2 T: Resolving Signatures of Surface Sites with Fast Magic Angle Spinning. *JACS Au* **2022**, *2* (11), 2460–2465.
(38) Lesage, A.; Lelli, M.; Gajan, D.; Caporini, M. A.; Vitzthum, V.; Miéville, P.; Alauzun, J.; Roussey, A.; Thieuleux, C.; Mehdi, A.; et al. Surface Enhanced NMR Spectroscopy by Dynamic Nuclear Polarization. *J. Am. Chem. Soc.* **2010**, *132* (44), 15459–15461.
(39) Liao, W.-C.; Ghaffari, B.; Gordon, C. P.; Xu, J.; Copéret, C. Dynamic Nuclear Polarization Surface Enhanced NMR Spectroscopy (DNP SENS): Principles, Protocols, and Practice. *Curr. Opin. Colloid Interface Sci.* **2018**, *33*, 63–71.
(40) Nagashima, H.; Trébosc, J.; Kon, Y.; Sato, K.; Lafon, O.; Amoureux, J.-P. Observation of Low-γ Quadrupolar Nuclei by Surface-Enhanced NMR Spectroscopy. *J. Am. Chem. Soc.* **2020**, *142* (24), 10659–10672.
(41) Venkatesh, A.; Hanrahan, M. P.; Rossini, A. J. Proton Detection of MAS Solid-State NMR Spectra of Half-Integer Quadrupolar Nuclei. *Solid State Nucl. Magn. Reson.* **2017**, *84* (January), 171–181.
(42) Jarupatrakorn, J.; Coles, M. P.; Tilley, T. D. Synthesis and Characterization of MO[OSi(OtBu)3] 4 and MO2[OSi(OtBu)3]2 (M = Mo, W): Models for Isolated Oxo-Molybdenum and -Tungsten Sites on Silica and Precursors to Molybdena- And Tungsta-Silica Materials. *Chem. Mater.* **2005**, *17* (7), 1818–1828.
(43) Nater, D. F.; Kaul, C. J.; Lätsch, L.; Tsurugi, H.; Mashima, K.; Copéret, C. Olefin Metathesis Catalysts Generated In Situ from Molybdenum(VI)-Oxo Complexes by Tuning Pendant Ligands. *Chem. - A Eur. J.* **2022**, *28* (22).
(44) Kamenar, B.; Penavić, M.; Korpar-Čolig, B.; Marković, B. Preparation and Crystal Structure of Two Oxo-Molybdenum Complexes with Dimethoxyethane. *Inorganica Chim. Acta* **1982**, *65* (C), 245–247.
(45) Becke, A. D. Density-Functional Thermochemistry. III. The Role of Exact Exchange. *J. Chem. Phys.* **1993**, *98* (7), 5648–5652.
(46) Hehre, W. J.; Ditchfield, K.; Pople, J. A. Self-Consistent Molecular Orbital Methods. XII. Further Extensions of Gaussian-Type Basis Sets for Use in Molecular Orbital Studies of Organic Molecules. *J. Chem. Phys.* **1972**, *56* (5), 2257–2261.
(47) Roy, L. E.; Hay, P. J.; Martin, R. L.; Roy, L. E.; Hay, P. J.; Martin, R. L. Revised Basis Sets for the LANL Effective Core Potentials Revised Basis Sets for the LANL Effective Core Potentials. *J. Chem. Theory Comput.* **2008**, *4* (7), 1029–1031.
(48) Perdew, J. P.; Burke, K.; Ernzerhof, M. Generalized Gradient Approximation Made Simple. *Phys. Rev. Lett.* **1996**, *77* (18), 3865–3868.
(49) Barbieri, P. L.; Fantin, P. A.; Jorge, F. E. Gaussian Basis Sets of Triple and Quadruple Zeta Valence Quality for Correlated Wave Functions. *Mol. Phys.* **2006**, *104* (18), 2945–2954.
(50) Lenthe, E. van; Baerends, E. J.; Snijders, J. G. Relativistic Regular Two-component Hamiltonians. *J. Chem. Phys.* **1993**, *99* (6), 4597–4610.
(51) Yakimov, A. V.; Ravi, M.; Verel, R.; Sushkevich, V. L.; van Bokhoven, J. A.; Copéret, C. Structure and Framework Association of Lewis Acid Sites in MOR Zeolite. *J. Am. Chem. Soc.* **2022**, *144* (23), 10377–10385.
(52) Edwards, J. C.; Adams, R. D.; Ellis, P. D. A 95Mo Solid-State NMR Study of Hydrodesulfurization Catalysts. 1. Formation of Fresh HDS Catalyst Precursors by Adsorption of Polyoxomolybdates onto γ-Alumina. *J. Am. Chem. Soc.* **1990**, *112* (23), 8349–8364.

(53) Haouas, M.; Trébosc, J.; Roch-Marchal, C.; Cadot, E.; Taulelle, F.; Martineau-Corcos, C. High-Field 95Mo and 183W Static and MAS NMR Study of Polyoxometalates. *Magn. Reson. Chem.* **2017**, *55* (10), 902–908.
(54) Sutter, K.; Autschbach, J. Computational Study and Molecular Orbital Analysis of NMR Shielding, Spin-Spin Coupling, and Electric Field Gradients of Azido Platinum Complexes. *J. Am. Chem. Soc.* **2012**, *134* (32), 13374–13385.
(55) Batista, P. R.; Ducati, L. C.; Autschbach, J. Solvent Effect on The195Pt NMR Properties in Pyridonate-Bridged PtIII Dinuclear Complex Derivatives Investigated By ab Initio Molecular Dynamics and Localized Orbital Analysis. *Phys. Chem. Chem. Phys.* **2021**, *23* (22), 12864–12880.
(56) Gordon, C. P.; Yamamoto, K.; Liao, W. C.; Allouche, F.; Andersen, R. A.; Copéret, C.; Raynaud, C.; Eisenstein, O. Metathesis Activity Encoded in the Metallacyclobutane Carbon-13 NMR Chemical Shift Tensors. *ACS Cent. Sci.* **2017**, *3* (7), 759–768.
(57) Gordon, C. P.; Raynaud, C.; Andersen, R. A.; Copéret, C.; Eisenstein, O. Carbon-13 NMR Chemical Shift: A Descriptor for Electronic Structure and Reactivity of Organometallic Compounds. *Acc. Chem. Res.* **2019**, *52* (8), 2278–2289.
(58) Staun, S. L.; Sergentu, D. C.; Wu, G.; Autschbach, J.; Hayton, T. W. Use of 15N NMR Spectroscopy to Probe Covalency in a Thorium Nitride. *Chem. Sci.* **2019**, *10* (26), 6431–6436.
(59) Du, J.; Seed, J. A.; Berryman, V. E. J.; Kaltsoyannis, N.; Adams, R. W.; Lee, D.; Liddle, S. T. Exceptional Uranium(VI)-Nitride Triple Bond Covalency from 15N Nuclear Magnetic Resonance Spectroscopy and Quantum Chemical Analysis. *Nat. Commun.* **2021**, *12*, 5649.
(60) Ramsey, N. F. Magnetic Shielding of Nuclei in Molecules. *Phys. Rev.* **1950**, *78* (6), 699–703.
(61) Liu, C. C.; Maciel, G. E. The Fumed Silica Surface: A Study by NMR. *J. Am. Chem. Soc.* **1996**, *118* (21), 5103–5119.
(62) Copéret, C.; Comas-Vives, A.; Conley, M. P.; Estes, D. P.; Fedorov, A.; Mougel, V.; Nagae, H.; Núnez-Zarur, F.; Zhizhko, P. A. Surface Organometallic and Coordination Chemistry toward Single-Site Heterogeneous Catalysts: Strategies, Methods, Structures, and Activities. *Chem. Rev.* **2016**, *116* (2), 323–421.
(63) Chan, K. W.; Lam, E.; D'Anna, V.; Allouche, F.; Michel, C.; Safonova, O. V.; Sautet, P.; Copéret, C. C-H Activation and Proton Transfer Initiate Alkene Metathesis Activity of the Tungsten(IV)-Oxo Complex. *J. Am. Chem. Soc.* **2018**, *140* (36), 11395–11401.
(64) Liu, S.; Boudjelel, M.; Schrock, R. R.; Conley, M. P.; Tsay, C. Interconversion of Molybdenum or Tungsten D2 Styrene Complexes with D01-Phenethylidene Analogues. *J. Am. Chem. Soc.* **2021**, *143* (41), 17209–17218.
(65) Wachs, I. E.; Roberts, C. A. Monitoring Surface Metal Oxide Catalytic Active Sites with Raman Spectroscopy. *Chem. Soc. Rev.* **2010**, *39* (12), 5002–5017.